Crystal structure and anti-site boundary defect characterisation in $Cu_2ZnSnSe_4$

BG Mendis[1], KP McKenna[2], G Gurieva[3], MS Rumsey[4] and S Schorr[3,5]

1. Dept. of Physics, Durham University, South Road, Durham, DH1 3LE, UK.
2. Dept. of Physics, University of York, Heslington, York, YO10 5DD, UK.
3. Dept. Structure and Dynamics of Energy Materials, Helmholtz-Zentrum Berlin für Materialien und Energie, Hahn-Meitner-Platz 1, 14109 Berlin, Germany.
4. Mineral and Planetary Sciences Division, Earth Sciences Department, Natural History Museum, Cromwell Road, London, SW7 5BD, UK.
5. Institute of Geological Sciences, Freie Universität Berlin, Malteserstraße 64-100, 12249 Berlin, Germany.

Abstract

Crystal structure identification of the photovoltaic material $Cu_2ZnSnSe_4$ (CZTSe) is challenging due to the distinguishing feature between the two polymorphs, kesterite and stannite, being the arrangement of Cu and Zn ions. Here an energy dispersive X-ray (EDX) technique, based on electron beam channeling along specific crystallographic planes in the transmission electron microscope (TEM), is used to identify the structure. Regions few 100 nm in size can be analysed using this method, unlike neutron or anomalous X-ray scattering. The parent crystal structure of CZTSe, annealed either side of the order-disorder transition temperature, was correctly identified as being kesterite. The presence of ½[110] (001) and ¼[201] (101) anti-site boundaries (ASB) have also been characterised. The density of ASBs is higher above the transition temperature, due to a smaller energy penalty for disordering on the 2c, 2d Wyckoff sites. A nearest neighbour cation analysis predicted the ½[110] (001) ASB to have the lowest formation energy. From density functional theory (DFT) simulations the ½[110] (001) ASB energy is only 43 mJ/m^2 and furthermore it is not a recombination site or current blocking layer, so that photovoltaic device performance is not significantly degraded.

Introduction

The adamantine compound $Cu_2ZnSn(S,Se)_4$, commonly abbreviated as CZTSSe or CZTS(e) depending on the composition, is a promising material for Tera Watt scale photovoltaic energy generation, since it is strongly light absorbing and consists entirely of earth abundant, cheap and non-toxic elements.[1] The record cell efficiency is however only 12.6% and defects within the material are thought to be a limiting factor.[2-3] In particular disorder of the Cu, Zn cations can lead to electrostatic and band gap fluctuations which limit the device efficiency.[4-11] The two most common crystal structures are kesterite (space group $I\bar{4}$) and stannite ($I\bar{4}2m$), which are both tetragonal and are shown in Figures 1a and 1b respectively. Kesterite is the lower energy structure, although the difference between the two is theoretically estimated to be only 0.3 eV/atom.[12] Using neutron diffraction and anomalous X-ray scattering on bulk materials Schorr and co-workers have confirmed that CZTS(e) forms as kesterite, but above a critical temperature of 203^{o}C the Cu, Zn atoms in the 2c and 2d sites, corresponding

to the z = ¼, ¾ planes (see Figure 1a), become fully disordered to give a structure with the same space group as stannite (Figure 1c).[13-14] The Cu atoms on the 2a sites (i.e. z = 0, ½ planes; Figure 1a) however remain ordered. The order-disorder transition is a second order phase transformation, so that in practice some disorder persists even below the critical temperature.[6]

Kattan *et al* recently reported two new types of anti-site boundaries (ASB) in CZTS kesterite nanoparticles grown using the hot injection method.[15] These are due to a ½[110] shear on a (001) plane and ¼[201] shear on a (101) plane respectively. A schematic of the two boundaries, as viewed along the [100] crystal projection, are shown in Figures 2a and 2b respectively. The ½[110] (001) boundary gives rise to Zn_{Cu} and Cu_{Zn} point defects on the 2c and 2d sites of the bottom half of the crystal, while the ¼[201] (101) boundary produces Sn_{Cu} anti-site atoms on 2c sites with respect to the top half of the crystal (for the latter Sn_{Zn} point defects are also possible if the perfect crystal is rotated 180^o about [100] prior to shear[15]). Both the ½[110] and ¼[201] vectors are consistent with ½<110> shear in the diamond cubic crystal structure, from which kesterite can be derived[16] (the $c/2a$ lattice parameter ratio for tetragonal kesterite and stannite is approximately unity). However, the ASB plane does not correspond to the {112} close packed plane. In fact for the ¼[201] (101) ASB there is a shear component normal to the boundary plane, meaning that material must be removed during its formation (in this case Cu atoms from the bottom crystal).[15]

Kesterite and stannite differ in the arrangement of Cu^+ and Zn^{2+} cations, so that it is not possible to identify the crystal structure using conventional X-ray and electron diffraction, since the number of electrons for the two ions are identical. Neutron diffraction and anomalous X-ray scattering are however not limited by this condition, but have other drawbacks such as the requirement of large volumes of material and/or access to expensive beam lines. Identifying the crystal structure is important, since it governs the point defect structure in the material, which in the case of kesterite gives rise to an order-disorder transition that directly impacts the efficiency of photovoltaic devices.[17] It is also not understood how the order-disorder transition influences the ASB defects in the material.

The aims of this paper are two-fold. First we employ a method for identifying the crystal structure of CZTSe that eliminates the above mentioned disadvantages of neutron and anomalous X-ray scattering. The method is an energy dispersive X-ray (EDX) analysis technique, known as ALCHEMI or **a**tom **l**ocation by **ch**anneling **e**nhanced **mi**croanalysis[18-19]. It requires only a standard transmission electron microscope (TEM) and the crystal structure can be determined from regions only a few 100 nm in size (e.g. individual grains in a thin-film device). Second, having used ALCHEMI to confirm the crystal structure of our samples as kesterite, we examine the role of order-disorder on ASB defects. TEM observations are supplemented with density functional theory (DFT) simulations to assess the impact of ASBs on device performance.

Experimental

Materials

In this paper bulk CZTSe powder samples are analysed. Unlike thin-films these samples are highly uniform in composition and have undergone extensive annealing to achieve thermodynamic equilibrium. This makes it ideal for investigating crystal structure and order-disorder effects. The samples were prepared by annealing the constituent elements (5N purity) in an evacuated quartz ampoule at 700^{o}C for 240 hours, followed by grinding in an agate mortar to homogenise the material and subsequently annealing at 700^{o}C for a further 240 hours. Small amounts of the material were then sealed in evacuated quartz ampoules, placed together in a furnace and given heat treatments at different temperatures, starting from high to low temperature, in order to induce varying degrees of disorder. Once a given anneal was complete one of the ampoules was rapidly removed from the furnace and quenched in ice water. In this paper samples annealed at 250^{o}C for 24 hours and 100^{o}C for 100 hours were analysed. Due to the nature of preparation the 100^{o}C annealed sample had also undergone the 250^{o}C/ 24 hour high temperature heat treatment. Wavelength dispersive X-ray (WDX) analysis in a scanning electron microscope showed the material to be Cu-poor (Cu/(Zn+Sn) = 0.96) and Zn-rich (Zn/Sn = 1.08) with no secondary phases. Further details can be found in reference [14].

In order to demonstrate the validity of the ALCHEMI method naturally occuring ferrokesterite and ferrostannite minerals, of composition $Cu_2(Fe,Zn)SnS_4$, were obtained on loan from the Natural History Museum in London, UK. These minerals contain Fe in Zn atom positions,[20] so that the Fe X-ray signal can be used to determine the sub-lattice through which the electron beam is being channelled (see Results and Discussion for further details). In practice the two minerals were found to be a mixture containing both kesterite and stannite phases, and therefore all results presented in this paper were from the sample labelled ‘ferrokesterite’ (Museum number BM 2016,25). The source of the mineral was the San Jose mine in Bolivia.

Electron Microscopy

CZTSe powder samples were ultrasonicated in isopropanol prior to being deposited on Mo grids with carbon support film. The ‘ferrokesterite’ mineral was finely crushed in an agate mortar, dispersed in isopropanol, and subsequently deposited on Mo grids with carbon film. A JEOL 2100F field emission gun TEM operating at 200 kV with Oxford INCA x-sight Si(Li) EDX detector was used for electron microscopy analysis, i.e. ALCHEMI experiments and ASB defect characterisation. The Mo grid did not affect the ALCHEMI measurements, since the Mo L background X-ray signal does not overlap with any of the Cu, Zn, Sn cation X-ray peaks. A 240 nm diameter area of the specimen was illuminated by the parallel electron beam during ALCHEMI measurements. The sample thickness was measured using the convergent beam electron diffraction (CBED) technique,[21] and was typically ~150 nm after tilting to the desired orientation.

Density functional theory simulations

To predict the structure, stability and electronic properties of the ½[110] (001) anti-site boundary (ASB) defect in CZTS and CZTSe we perform first principles calculations using density functional theory. We employ the projector augmented wave method as implemented

in the Vienna *ab initio* simulation package[22-23] together with the Heyd, Scuseria, and Ernzerhof (HSE) hybrid exchange-correlation (XC) functional,[24] which gives much improved predictions with respect to band gaps compared to standard local or semi-local XC functionals. The 3*p*, 3*d* and 4*s* electrons of Cu, 3*d* and 4*s* electrons of Zn, 4*d*, 5*s* and 5*p* electrons of Sn, 3*s* and 3*p* electrons of S, and 4*s* and 4*p* electrons of Se are treated as valence electrons and expanded in a plane wave basis with energies up to 500 eV. For the calculation of bulk kesterite properties we use the 16-atom conventional unit cell with a gamma point centred 8 x 8 x 4 Monkhorst-Pack (MP) grid to sample the Brillouin zone. The Fock exchange potential is sampled using a coarser 4 x 4 x 2 MP grid. The total energy is optimised with respect to the position of atoms and the unit cell dimensions using a conjugate gradients algorithm until all forces are less than 0.01 eV $Å^{-1}$. Using this approach we predict properties of bulk Cu_2ZnSnS_4 (a=5.435 Å, c=10.856 Å, E_g=1.47 eV) and $Cu_2ZnSnSe_4$ (a=5.715 Å, c=11.412 Å, E_g=0.91 eV) in good agreement with previous calculations and experiment.[25,26]

To model the ASB defects we expand the conventional unit cell into a 1 x 1 x 6 supercell (96 atoms in total) and displace half of the atoms in the supercell by ½[110] creating two equally spaced ASBs. The separation between the periodically repeating ASBs is > 30 Å, ensuring that artificial interactions are minimised. The structure of the supercell is optimised using the same methods described for the bulk but with the MP grid reduced to 3 x 3 x 1. A similar approach was employed recently to model anti-phase boundary defects in Fe_3O_4.[27] The total energy is also calculated for a 1 x 1 x 6 supercell without the ASB displacement (corresponding to a bulk crystal) in order to calculate the ASB formation energy.

Results and Discussion

ALCHEMI results

When a crystal is tilted close to two-beam conditions, such that only a single Bragg beam is excited along with the unscattered beam, the incident electrons in the TEM will channel either along or between the Bragg diffracting planes, the nature of the channeling depending on the precise specimen orientation.[18-19] If the incident angle of the TEM electrons is smaller than the Bragg angle, i.e. so-called negative deviation parameter,[28] then channeling largely takes place along the diffracting crystal plane, while for incident angles larger than the Bragg angle (i.e. positive deviation parameter) channeling is largely between the crystal planes. EDX spectra acquired under negative deviation parameter conditions therefore show increased X-ray signal from those elements that make up the crystal plane of interest. This is the origin of the ALCHEMI effect. It can be used to distinguish between the kesterite and stannite phases. For example, assume that Bragg diffraction is due to the (002) planes. At negative deviation parameter channeling is therefore along the z = 0, ½ planes containing Sn atoms (Figure 1). The other cation within these planes is Cu for kesterite, and Zn for stannite. On the other hand for positive deviation parameter channeling is along the z = ¼, ¾ planes, which consists of equal amounts of Cu and Zn for kesterite and pure Cu for stannite. Thus for kesterite the (Zn/Cu) ratio is smaller for the EDX spectrum acquired under negative deviation parameter compared to positive deviation parameter, while the opposite is true for stannite.

Examination of the crystal structures in Figure 1 show that the same effect must be observed if the diffracting plane is (110) rather than (002).

Although channeling can distinguish between kesterite and stannite phases it cannot however distinguish between the ordered and disordered states of kesterite, since disorder occurs amongst the 2c (Cu) and 2d (Zn) sites within the z = ¼, ¾ crystal planes, while the 2a (Cu) sites remain ordered.[14] Hence what is determined is the *parent* crystal structure, i.e. for a fully disordered kesterite, with the same $I\bar{4}2m$ space group as stannite, the ALCHEMI method would identify the crystal structure as being kesterite, but provide no information on the degree of disorder. Bosson *et al* have reported that for Sn-poor, Zn-rich CZTS (i.e. Cu/(Zn+Sn) = 0.97, Zn/Sn = 1.62) approximately one third of the Cu 2a kesterite sites are occupied by Zn;[29] although this does not preclude crystal structure identification it does mean that there would be less variation between EDX spectra acquired under different channeling conditions, thus placing greater demands on the signal to noise ratio of the ALCHEMI measurement.

In practice it is difficult to satisfy two-beam conditions due to the large unit cell, and what is observed is many-beam excitation along a systematic row. Meaningful results are nevertheless obtained for EDX spectra acquired in the symmetry orientation (i.e. incident electron beam parallel to the diffracting planes) and with a slightly positive deviation parameter of ~0.005 nm^{-1} from the 008 or 220 higher order Bragg condition. Bloch wave calculations[28] of the electron wavefunction within the crystal confirm these observations. Figures 3a and 3b show the depth integrated electron intensity along the [001] crystal direction for a 150 nm thick kesterite specimen tilted to the symmetry orientation and near (i.e. 0.005 nm^{-1} deviation parameter) 008 Bragg condition respectively. Note that what is plotted here is the elastic electron intensity integrated through the specimen thickness. The spatial distribution of thermal diffuse scattered (TDS) electrons cannot be calculated using a Bloch wave simulation, although the TDS contribution to the channeling signal is expected to be comparatively smaller due to its more delocalised nature. Comparing integrated electron intensities along the z = 0, ½ planes containing 2a, 2b atom sites with the z = ¼, ¾ planes containing 2c, 2d sites, the former is found to be relatively higher for the symmetry orientation (Figure 3a), while the latter is relatively higher near the 008 Bragg condition (Figure 3b). Although the integrated electron intensities for the many-beam scenario, particularly near the 008 Bragg condition, does not strictly follow the predictions of two-beam theory discussed earlier, the channeling is nevertheless sufficiently similar to the ideal two-beam case for the purpose of distinguishing crystal structure. Furthermore, the integrated electron intensity along the [110] crystal direction for a 150 nm thick kesterite specimen tilted to the symmetry orientation and near (i.e. 0.005 nm^{-1} deviation parameter) 220 Bragg condition are shown in Figures 3c and 3d respectively. The channeling is similar to Figures 3a and 3b, confirming the suitability of these diffraction conditions for ALCHEMI measurements. Although results for only a 150 nm thick kesterite specimen are presented here, calculations for other specimen thicknesses (i.e. 50, 100 and 200 nm) showed similar trends. The conclusions were also found to be valid for the stannite phase.

The ALCHEMI method is first demonstrated on the $Cu_2(Fe,Zn)SnS_4$ 'ferrokesterite' mineral, since the Fe X-ray signal can be used to confirm the sub-lattice through which the electron

beam is channeling. Figures 4a and 4b show the results for kesterite and stannite phases in the 'ferrokesterite' mineral. In each figure the EDX spectrum acquired at symmetry orientation is superimposed with that acquired close to the 008/220 higher order Bragg condition. The Cu Kα X-ray intensity is normalised for direct comparison and the intensity scale has been expanded so that the full Cu Kα peak is not visible. For both kesterite and stannite phases the Sn L X-ray signal is higher in the symmetry orientation, due to the electron beam preferentially channeling along the planes containing 2b (Sn) sites. The EDX spectrum from near the higher order Bragg condition shows a relative increase in the Fe Kα and Zn Kα X-ray signal for the kesterite phase (Figure 4a) and a relative decrease for stannite (Figure 4b). These observations are consistent with the fact that for these specimen orientations there is a larger EDX signal from planes containing 2c (Cu), 2d (Zn) sites in kesterite, and 4d (Cu) sites in stannite. Fe occupies the Zn sub-lattice and therefore the X-ray signal for the two elements show similar intensity variations with respect to channeling.

The successful demonstration of the ALCHEMI method on a $Cu_2(Fe,Zn)SnS_4$ test sample means that it can now be applied to the CZTSe bulk powder samples. Figures 4c and 4d show representative ALCHEMI results for CZTSe annealed at 250^{o}C and 100^{o}C respectively (the figures have been plotted in a similar manner to Figures 4a and 4b). Previous anomalous X-ray scattering results on these same samples have shown that at 250^{o}C the Cu, Zn cations on the 2c and 2d crystallographic sites in the parent kesterite structure are completely disordered (0.5 site occupation factor), while at 100^{o}C partial ordering is restored, such that the site occupation factor increases to ~0.8.[14] The Cu atoms on the 2a sites remain almost fully ordered, even at high temperature. In both Figures 4c and 4d the Zn Kα X-ray signal has higher intensity when acquired near the higher order Bragg condition, which is consistent with a parent kesterite crystal structure (recall that the ALCHEMI technique is not sensitive to ordering of the 2c, 2d sites). Measurements were carried out on at least three grains for each heat treatment temperature, and in all cases the results indicated a kesterite phase, in agreement with anomalous X-ray scattering.[14] The advantage of ALCHEMI however is that the measurements were carried over regions a few 100 nm in size. This opens up new possibilities, such as analysing the crystal structure of individual grains in a thin-film device.

Anti-site boundary imaging

In this section the presence of ¼[201] (101) and ½[110] (001) anti-site boundaries in the CZTSe bulk powder samples, annealed at 250^{o}C and 100^{o}C, is reported. As described in reference [15] the ¼[201] (101) boundaries are visible using **g** = 002 TEM dark-field imaging (any ½[110] (001) boundaries are however invisible). Alternating black and white interference fringes are observed along the projection of the inclined ASB plane, due to the ¼[201] shear causing a phase shift of the **g** = 002 diffracted beam relative to the unscattered beam.[28] Figures 5a and 5b show ¼[201] (101) ASBs in two different particles of the 250^{o}C annealed sample. The dark-field images were acquired close to the [110] zone-axis; the measured angle between the **g** = 002 diffracting vector and trace of the ASB is consistent with a (101) habit plane. Note that the angle is also consistent with a $(1\,\bar{1}\,2)$ close packed plane, although this habit plane can be ruled out since the ASBs would be approximately end-on and should not therefore exhibit significant black-white interference fringes. **g** = 002 dark-field images for the 100^{o}C annealed sample are shown in Figures 5c and 5d and did not

reveal any ¼[201] (101) ASBs. Recall that the 100°C sample had also undergone the same high temperature heat treatment at 250°C (see Experimental section), and therefore had the same starting ASB defect population as the 250°C sample. All three particles analysed in the 250°C sample showed ¼[201] (101) ASBs, while for the 100°C sample ASBs were not detected in five particles analysed. These are small numbers, and is due to the laborious process of finding particles that can be tilted to the desired orientation. Nevertheless the apparent scarcity of ASBs at low temperature suggests that they become unstable with respect to ordering of the bulk crystal.

½[110] (001) ASBs can be revealed using **g** = 101 dark field imaging. Of the major zone axes in CZTSe however the 101 reciprocal vector is found only along the [010] direction. At this specimen orientation the ASBs are end-on, so that lattice imaging, using high resolution electron microscopy (HREM), is more appropriate for characterising the defects. Figure 6a is an HREM image of the 250°C annealed CZTSe sample along [010], and shows a high density of ½[110] (001) ASBs. The HREM image has a limited field of view, but the selected area electron diffraction pattern for the same particle, shown in Figure 6b, exhibits streaking along the 002 reciprocal direction. The streaking is due to the shape transform of the two-dimensional ASB in reciprocal space (i.e. relrod[28]) and indicates a high density of such defects over a larger area than that observed in the HREM image. Figure 6c is the corresponding [010] HREM image for the 100°C annealed CZTSe sample. No ASBs are visible and the selected area diffraction pattern in Figure 6d does not show any streaking, which suggests that the ½[110] (001) ASBs become less abundant with ordering of the bulk crystal. The statistics however are poor, i.e. only one and two particles were analysed for the 250°C and 100°C samples respectively.

The scarcity of ¼[201] (101) and ½[110] (001) ASBs at the lower annealing temperature suggests that the boundary energy increases for the ordered crystal. This can be explained by examining the structure of the two ASBs, as shown in Figures 2a and 2b. In both cases the anti-site atoms and vacancies are at the 2c, 2d Wyckoff positions. For the ½[110] (001) ASB there are Zn_{Cu} and Cu_{Zn} anti-site atoms with respect to the bottom half of the crystal (Figure 2a). For the ¼[201] (101) boundary the defects are Sn_{Cu} on 2c sites in the top half of the crystal and furthermore Cu atoms are removed from the 2c sites of the bottom crystal, due to the shear component normal to the boundary plane (Figure 2b). As the annealing temperature is lowered below the critical ordering temperature the Gibbs energy of such 2c, 2d anti-site atoms and vacancies increase, thereby increasing the ASB energy.

It is interesting that the habit plane of the ASBs do not correspond to {112}, i.e. the close packed plane in the parent diamond cubic crystal structure on which shear is comparatively easy.[30] HREM images were also acquired along the [201] zone-axis, since in this orientation two out of the four unique {112} planes are end-on. i.e. $(11\bar{2})$ and $(\bar{1}12)$. Three particles in the 250°C sample and two particles in the 100°C sample were analysed, and only one isolated defect with {112} habit plane was detected in the latter. For a ½[110] or ¼[201] shear the preferred habit plane is therefore not {112}. This can be easily explained for the ½[110] (001) ASB. Table 1 lists the nearest neighbour cations for Cu, Zn and Sn in bulk kesterite. The twelve nearest neighbours are along the ½<110> directions in the parent diamond cubic crystal. Examination of Figure 2a reveals that the same nearest neighbour cations are

preserved for the ½[110] (001) ASB, and consequently its formation energy should be low, a fact confirmed by DFT simulations (see next section). Compare this with a ½<110> shear along the {112} plane, where the nearest neighbour cations are not preserved. This is evident from Figure 7 which shows the structure of the {112} cation plane in kesterite. A ½[110] shear, the same as the ½[110] (001) ASB, shifts a cation on the close packed layer above (dashed circle) along the blue arrow indicated in the figure. In this particular case Sn is substituted for Cu as one of the nearest neighbours for the displaced cation. It may be argued that a 1/12[241] shear, equivalent to a 1/6[121] shear in the diamond cubic crystal, is more likely along the {112} plane. The shear is indicated by the red arrow in Figure 7 and it is clear that the resulting nearest neighbours are the same as for a ½[110] shear. Examination of the ¼[201] (101) ASB in Figure 2b shows that the nearest neighbour cations are also not preserved. Thus this defect, as well as ASBs on {112} habit planes, are expected to have relatively higher formation energies. Nevertheless the importance of {112} ASBs must not be entirely ruled out. Our preliminary investigations on a CZTS thin-film device revealed a high density of {112} twins in certain grains (see also reference [31]). This could be caused by strain build up in the CZTS layer during film growth; the strain is most readily relieved by shearing the {112} close packed planes, where the Peierls-Nabarro stress for dislocation glide is minimal.[30] The CZTSe powder in this study and CZTS nanoparticles in reference [15] are however free standing, so that strain considerations do not apply.

Density functional theory calculations

DFT calculations are performed for the ½[110] (001) ASB, since this is predicted to have the lowest formation energy. The optimised structure of the CZTSe ASB supercell (see Experimental section) is shown in Figure 8. The ASB causes very little perturbation in the atomic structure, with atoms at the interface retaining the same coordination and very similar bond lengths to the perfect crystal. The formation energy (E_f) of the ASB is calculated using,

$$E_f = (E_{ASB} - E_{bulk})/2A \quad \ldots (1)$$

where E_{ASB} is the total energy of the supercell containing the ASBs, E_{bulk} is the total energy of the same supercell without the ASBs present and A is the cross sectional area of the supercell (the factor of two arises due to the fact there are two ASBs in the supercell). The formation energy of the ½[110] (001) ASB in CZTSe is found to be only 43 mJ/m^2. This extremely low value is consistent with the small structural perturbation that is observed and suggests such defects may form easily. We have also optimised the structure of the CZTS ASB and find an almost identical structure to that shown in Figure 8. However, the formation energy is slightly lower (35 mJ/m^2).

Next we address the electronic properties of the CZTSe ASB defect. We characterise the electronic structure of the ASB by calculating the local density of states (LDOS) in a region of width 4 Å centered on one of the ASBs and in the centre of the bulk region. The two LDOS are shown in Figure 9a along with a reference density of states calculated for the bulk crystal supercell. The ASBs are found to introduce no new states into the gap near the valence band maximum or conduction band minimum. Therefore the ASB would appear to be relatively benign for carrier transport as it does not represent a Shockley-Read-Hall (SRH)

recombination site for electrons or holes. In fact the LDOS in the bulk and ASB regions are remarkably similar across a wide range of energies. The only significant difference appears above the conduction band minimum, at around 1.5 and 2.1 eV, where electronic states at the ASB appear to be slightly deeper than the corresponding states in the bulk region. These resonant states may play some role for the transport of hot electrons, but given the relatively fast relaxation of hot electrons should not impact significantly on device performance. Furthermore, the absence of a band offset between ASB and bulk crystal for both valence and conduction bands means that the defects do not act as electron/hole current blocking layers, cf. ZnSe in CZTSe[32] or grain boundary hole barriers in $CuInSe_2$ (CIS)[33].

The LDOS for the CZTS ASB defect is almost identical, albeit with a larger band gap (Figure 9b). Again there are no localised states associated with the ASB inside the band gap. The resonant states in the conduction band occur at higher energies of 2.0 and 2.6 eV. As for CZTSe the conclusion is that the ½[110] (001) ASB in CZTS does not represent a SRH recombination centre and has no band discontinuities and should therefore be benign for device performance.

Summary

In the ALCHEMI technique TEM-EDX spectra are acquired under diffraction conditions that induce channeling of the electron beam along certain crystallographic planes. It can be used to identify the parent crystal structure of CZTS(e) within regions few 100 nm in size, which is otherwise not possible using standard techniques such as neutron diffraction and anomalous X-ray scattering. As proof of principle ALCHEMI has been applied to identify the kesterite and stannite phases in a $Cu_2(Fe,Zn)SnS_4$ mineral, where the Fe X-ray signal can be used to monitor channeling or non-channeling of the electron beam along the Zn sub-lattice. The technique was also used to characterise CZTSe powder samples annealed either side of the order-disorder temperature, and confirmed the parent crystal structure to be kesterite, consistent with previous anomalous X-ray scattering results.

½[110] (001) and ¼[201] (101) ASBs, previously reported for CZTS nanoparticles, have also been observed in the CZTSe powder samples. The ASB density is however lower for the ordered sample, suggesting that the Gibbs energy of the defects increase as the material is cooled below the order-disorder transition temperature. This can be related to the ASB shear induced, anti-site atoms and/or vacancies at the 2c, 2d Wyckoff positions. An analysis of the nearest neighbour cations predicts that the ½[110] (001) ASB has the lowest formation energy. From DFT calculations the formation energy of the ½[110] (001) ASB in CZTSe is only 43 mJ/m^2 (35 mJ/m^2 for CZTS). Although there is a low energy barrier for creating ½[110] (001) defects the coordination environment is similar to the perfect crystal, at least for the nearest neighbour cations, so that there are no localised electronic states within the band gap and no valence/conduction band discontinuities. The ½[110] (001) ASBs are therefore not Shockley-Read-Hall recombination sites or current blocking layers, and will not have any significant influence on photovoltaic device performance.

Conflicts of interest

There are no conflicts of interest to declare.

Acknowledgements

KPM acknowledges support from EPSRC (EP/K003151/1 and EP/P023843/1). This work made use of the facilities of Archer, the UK's national high-performance computing service, via our membership in the UK HPC Materials Chemistry Consortium, which is funded by EPSRC (EP/L000202). All data relating to the density functional theory calculations created during this research are available by request from the University of York Research database (https://doi.org/10.15124/c0cd73d0-ec8e-4eda-abeb-4e9dd5cd3b3f).

References

1. K Ito, *Copper Zinc Tin Sulfide-Based Thin Film Solar Cells*, Wiley, United Kingdom (2015).
2. MA Green, K Emery, Y Hishikawa, W Warta and ED Dunlop, *Prog. Photovolt: Res. Appl.* **25** (2017) 668.
3. X Liu, Y Feng, H Cui, F Liu, X Hao, G Conibeer, DB Mitzi and M Green, *Prog. Photovolt: Res. Appl.* **24** (2016) 879.
4. JH Werner, J Mattheis and U Rau, *Thin Solid Films* **480** (2005) 399.
5. T Gokmen, O Gunawan, TK Todorov and DB Mitzi, *Appl. Phys. Lett.* **103** (2013) 103506.
6. JJS Scragg, L Choubrac, A Lafond, T Ericson and C Platzer-Björkman, *Appl. Phys. Lett.* **104** (2014) 041911.
7. G Rey, A Redinger, J Sendler, TP Weiss, M Thevenin, M Guennou, BE Adib and S Siebentritt, *Appl. Phys. Lett.* **105** (2014) 112106.
8. DP Halliday, R Claridge, MCJ Goodman, BG Mendis, K Durose and JD Major, *J. Appl. Phys.* **113** (2013) 223503.
9. BG Mendis, MD Shannon, MCJ Goodman, JD Major, R Claridge, DP Halliday and K Durose, *Prog. Photovolt: Res. Appl.* **22** (2014) 24.
10. JA Aguiar, ME Erkan, DS Pruzan, A Nagaoka, K Yoshino, H Moutinho, M Al-Jassim and MA Scarpulla, *Phys. Status Solidi A* **213** (2016) 2392.
11. BG Mendis, AA Taylor, M Guennou, DM Berg, M Arasimowicz, S Ahmed, H Deligianni and PJ Dale, *Sol. Energy Mater. Sol. Cells* **174** (2018) 65.
12. S Chen, XG Gong, A Walsh and S-Huai Wei, *Appl. Phys. Lett.* **94** (2009) 041903.
13. S Schorr, H-J Hoebler and M Tovar, *Eur. J. Mineral.* **19** (2007) 65.
14. DM Többens, G. Gurieva, S Levcenko, T Unold and S Schorr, *Phys. Status Solidi B* **253** (2016) 1890.
15. NA Kattan, IJ Griffiths, D Cherns and DJ Fermin, *Nanoscale* **8** (2016) 14369.
16. S Schorr, *Thin Solid Films* **515** (2007) 5985.
17. G Rey, TP Weiss, J Sendler, A Finger, C Spindler, F Werner, M Melchiorre, M Hála, M Guennou and S Siebentritt, *Sol. Energy Mater. Sol. Cells* **151** (2016) 131.
18. JCH Spence and J Taftø, *J. Microsc.* **130** (1983) 147.
19. IP Jones, *Adv. Imaging Electron Phys.* **125** (2002) 63.
20. P Bonazzi, L Bindi, GP Bernardini and S Menchetti, *Canadian Mineralogist* **41** (2003) 639.

21. IP Jones, *Chemical microanalysis using electron beams*, The Institute of Materials, London (1992).
22. G Kresse and J Furthmüller, *Phys. Rev. B* **54** (1996) 11169.
23. G Kresse and J Furthmüller, *J. Comput. Mater.* **6** (1996) 15.
24. J Heyd, GE Scuseria and M Ernzerhof, *J. Chem. Phys.* **118** (2003) 8207.
25. J Paier, R Asahi, A Nagoya and G Kresse, *Phys. Rev. B* **79** (2009) 115126.
26. YS Yee, B Magyari-Köpe, Y Nishi, SF Bent and BM Clemens, *Phys. Rev. B* **92** (2015) 195201.
27. KP McKenna, F Hofer, D Gilks, VK Lazarov, C Chen, Z Wang and Y Ikuhara, *Nature Communications* **5** (2014) 5740.
28. PB Hirsch, A Howie, RB Nicholson, DW Pashley and MJ Whelan, *Electron Microscopy of Thin Crystals*, Butterworths, Great Britain (1965).
29. CJ Bosson, MT Birch, DP Halliday, KS Knight, AS Gibbs and PD Hatton, *J. Mat. Chem. A* **5** (2017) 16672.
30. D Hull and DJ Bacon, *Introduction to Dislocations*, Butterworth-Heinemann, Oxford (2001).
31. J Ge, J Jiang, P Yang, C Peng, Z Huang, S Zuo, L Yang and J Chu, *Sol. Energy Mater. Sol. Cells* **125** (2014) 20.
32. JT Wätjen, J Engman, M Edoff and CP Björkman, *Appl. Phys. Lett.* **100** (2012) 173510.
33. C Persson and A Zunger, *Phys. Rev. Lett.* **91** (2003) 266401.

Tables

Ion	Nearest neighbour cations
Cu (2a, 2c sites)	4 Cu, 4 Zn, 4 Sn
Zn (2d)	8 Cu, 4 Sn
Sn (2b)	8 Cu, 4 Zn

Table 1: List of the twelve nearest neighbour cations for Cu, Zn and Sn ions in the kesterite crystal structure.

Figures

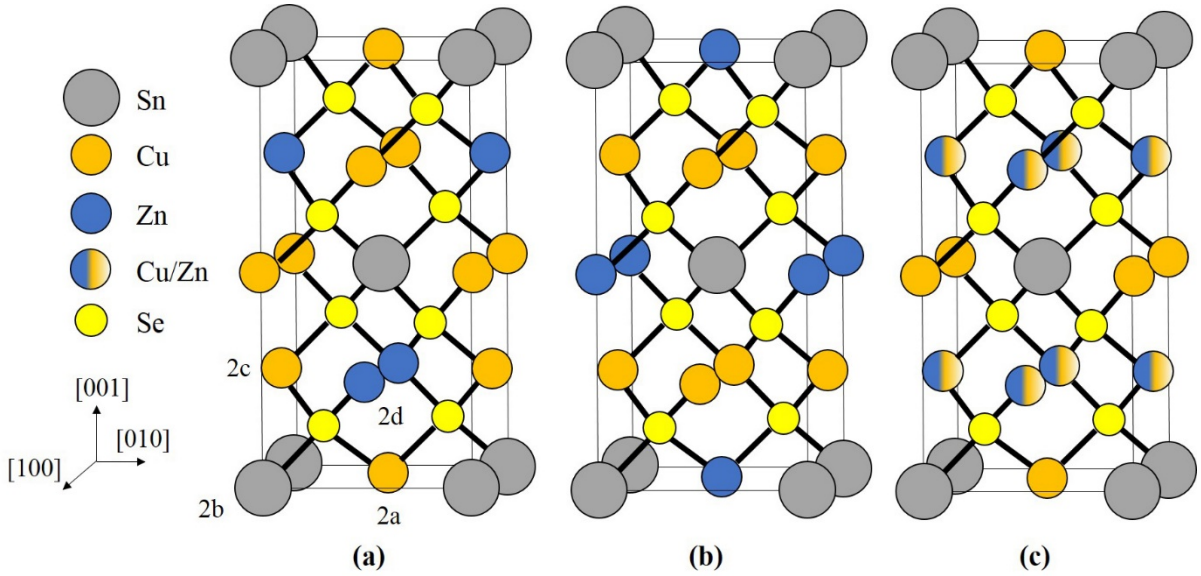

Figure 1: Crystal structure of (a) ordered kesterite, (b) stannite and (c) disordered kesterite. Example 2a (Cu), 2b (Sn), 2c (Cu) and 2d (Zn) Wyckoff positions in kesterite are indicated in (a). In disordered kesterite the 2c and 2d atom positions in the z = ¼, ¾ planes are mixed, with equal occupancies of Cu and Zn.

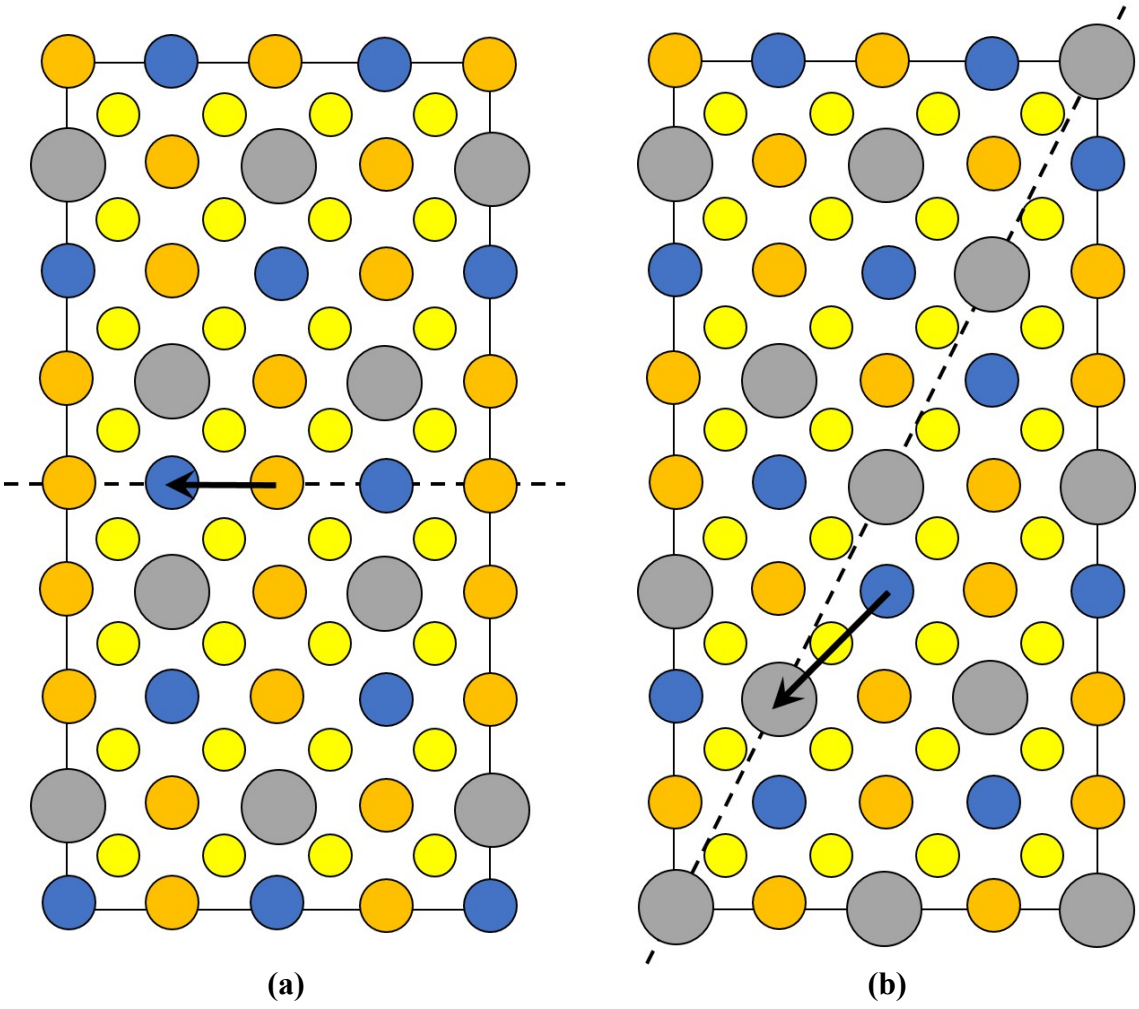

Figure 2: Supercell of the (a) ½[110] (001) and (b) ¼[201] (101) ASBs in kesterite viewed along [100] (the vertical axis is [001], while the horizontal axis is [010]). Cu, Zn, Sn and Se

atoms are depicted by orange, blue, silver and yellow circles respectively. The dashed line represents the ASB plane and the arrow the ASB shear vector projected onto the [100] viewing plane. In both figures the bottom half of the crystal is displaced with respect to the top half. Figures adapted from reference [15].

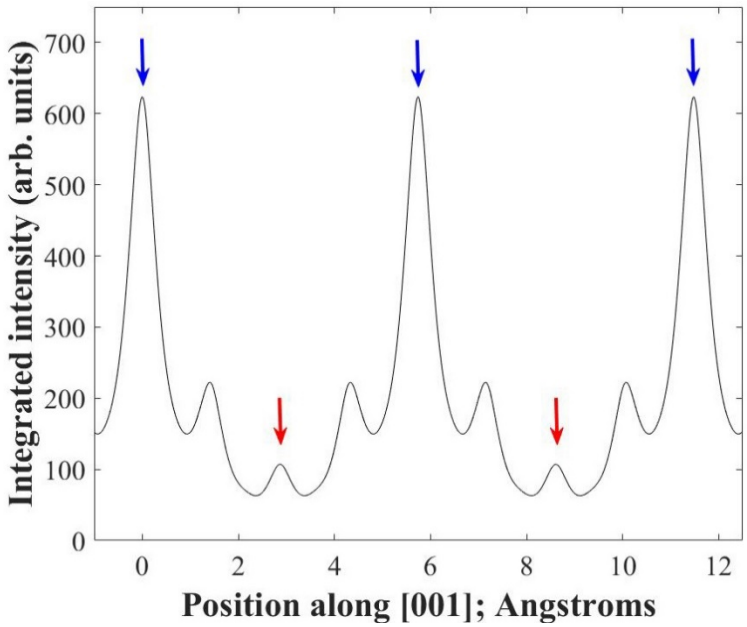

(a)

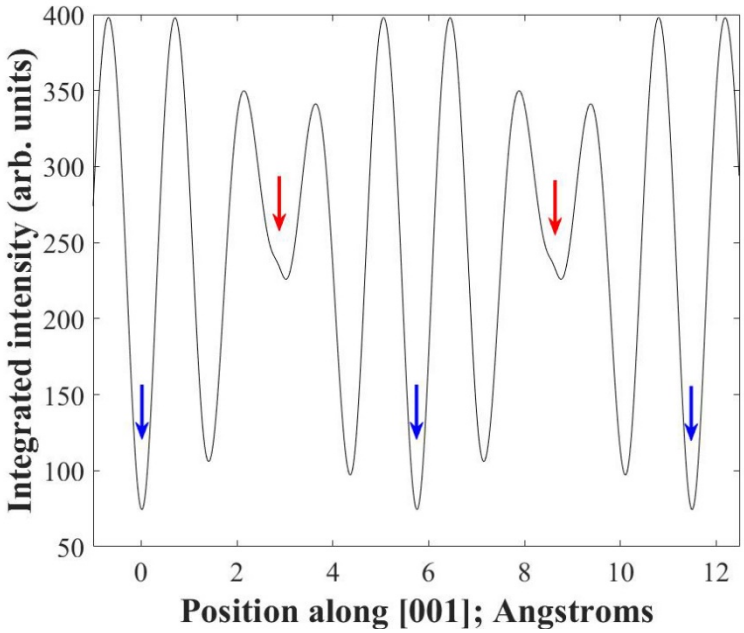

(b)

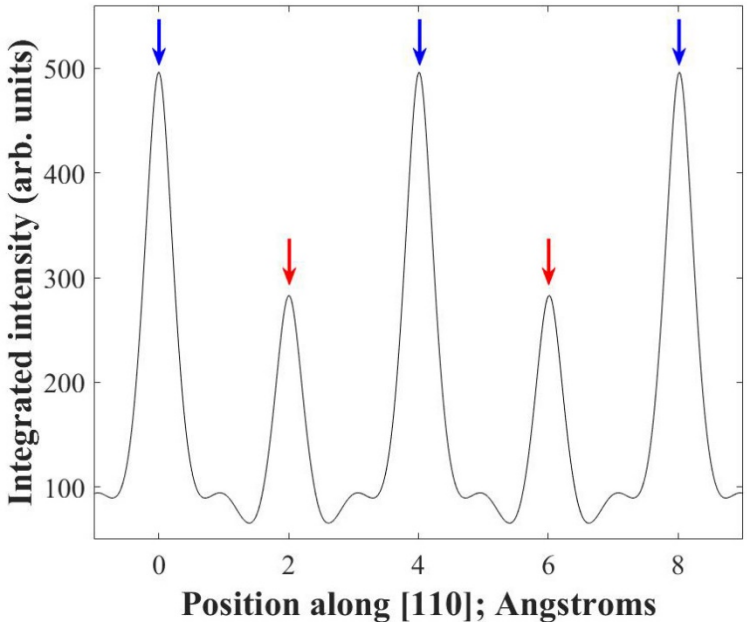

(c)

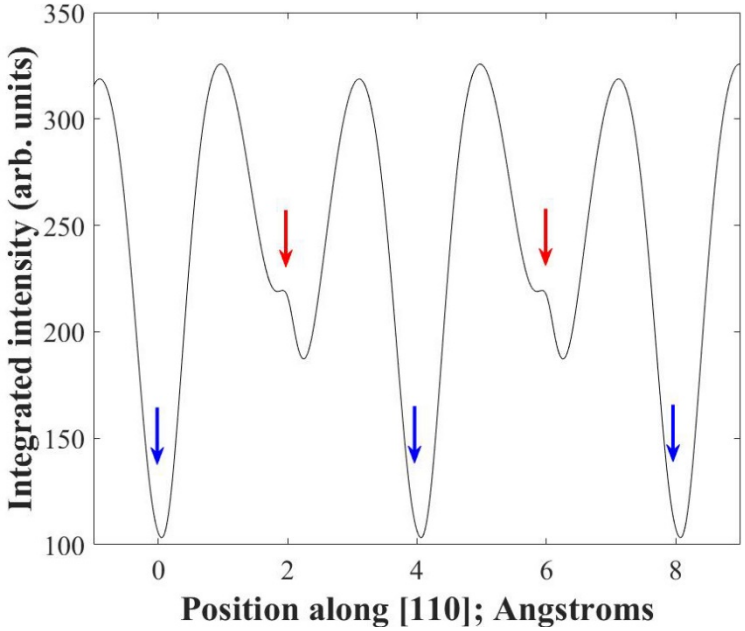

(d)

Figure 3: Bloch wave calculated, elastic electron intensity integrated through the thickness of a 150 nm thick $Cu_2ZnSnSe_4$ kesterite specimen. In (a) the specimen is at the symmetry orientation of the 002 reciprocal vector systematic row, while in (b) the specimen is near (i.e. 0.005 nm^{-1} deviation parameter) to the 008 Bragg condition. The integrated intensity is plotted along the [001] crystal direction. In (c) the specimen is at the symmetry orientation of the 110 reciprocal vector systematic row, while in (d) the specimen is near (i.e. 0.005 nm^{-1} deviation parameter) to the 220 Bragg condition. The integrated intensity is plotted along the [110] crystal direction. Blue and red arrows indicate positions of planes containing 2a, 2b and 2c, 2d atom sites respectively.

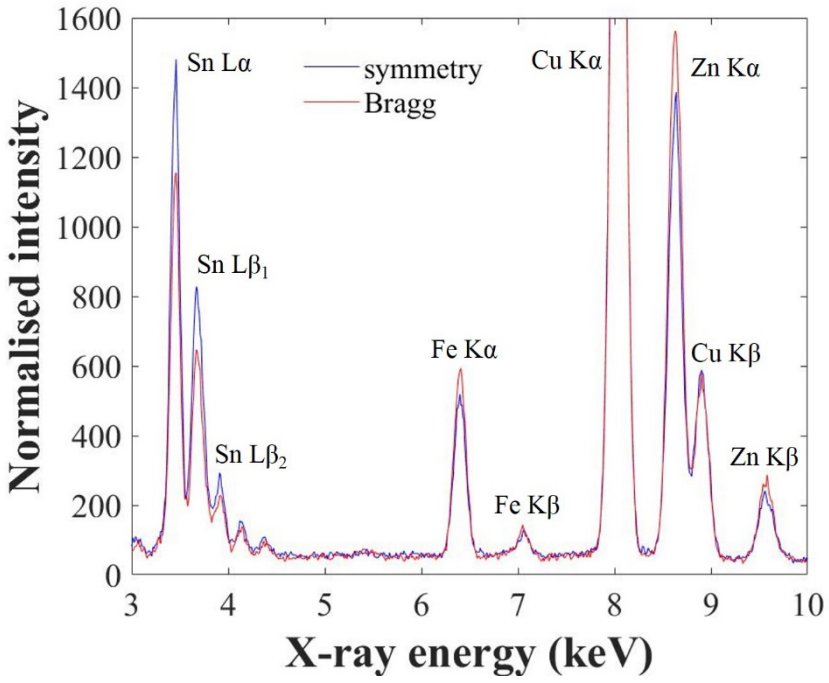
Normalised intensity
X-ray energy (keV)
symmetry
Bragg
Sn Lα
Sn Lβ1
Sn Lβ2
Fe Kα
Fe Kβ
Cu Kα
Cu Kβ
Zn Kα
Zn Kβ

(a)

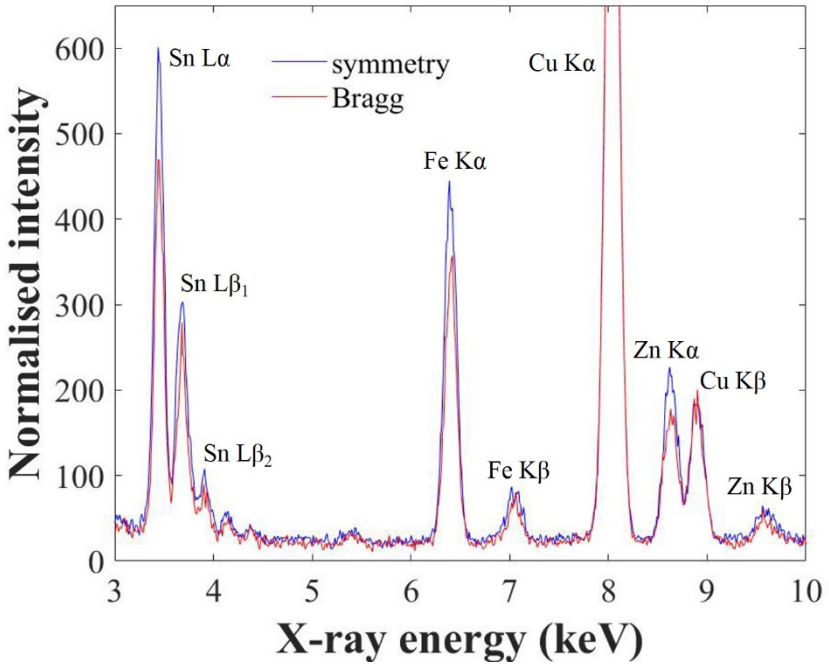
Normalised intensity
X-ray energy (keV)
symmetry
Bragg
Sn Lα
Sn Lβ1
Sn Lβ2
Fe Kα
Fe Kβ
Cu Kα
Cu Kβ
Zn Kα
Zn Kβ

(b)

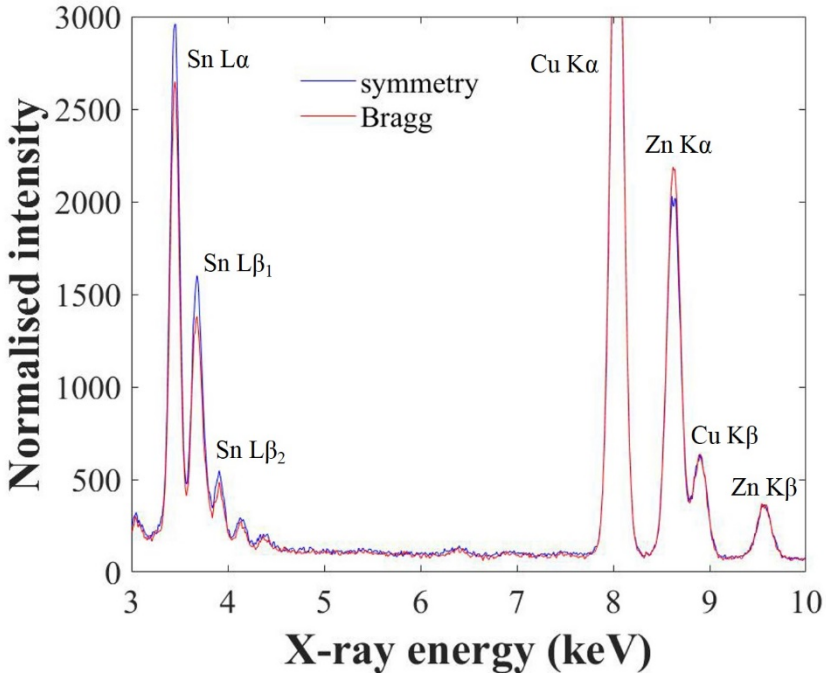

(c)

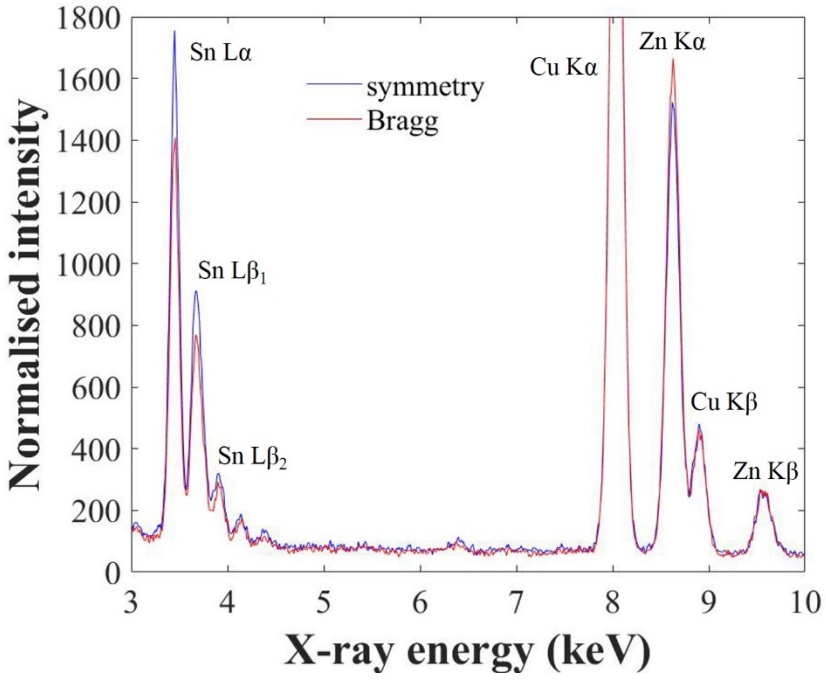

(d)

Figure 4: ALCHEMI results for (a) kesterite and (b) stannite phase in a $Cu_2(Fe,Zn)SnS_4$ mineral. In each figure EDX spectra for the symmetry orientation and near 008/220 high order Bragg condition are superimposed. The Cu Kα peak intensity is normalised for direct comparison and the intensity scale has been expanded, so that the Cu Kα peak is not fully visible. The corresponding results for the $Cu_2ZnSnSe_4$ powder sample annealed at 250^{o}C and 100^{o}C are shown in (c) and (d) respectively.

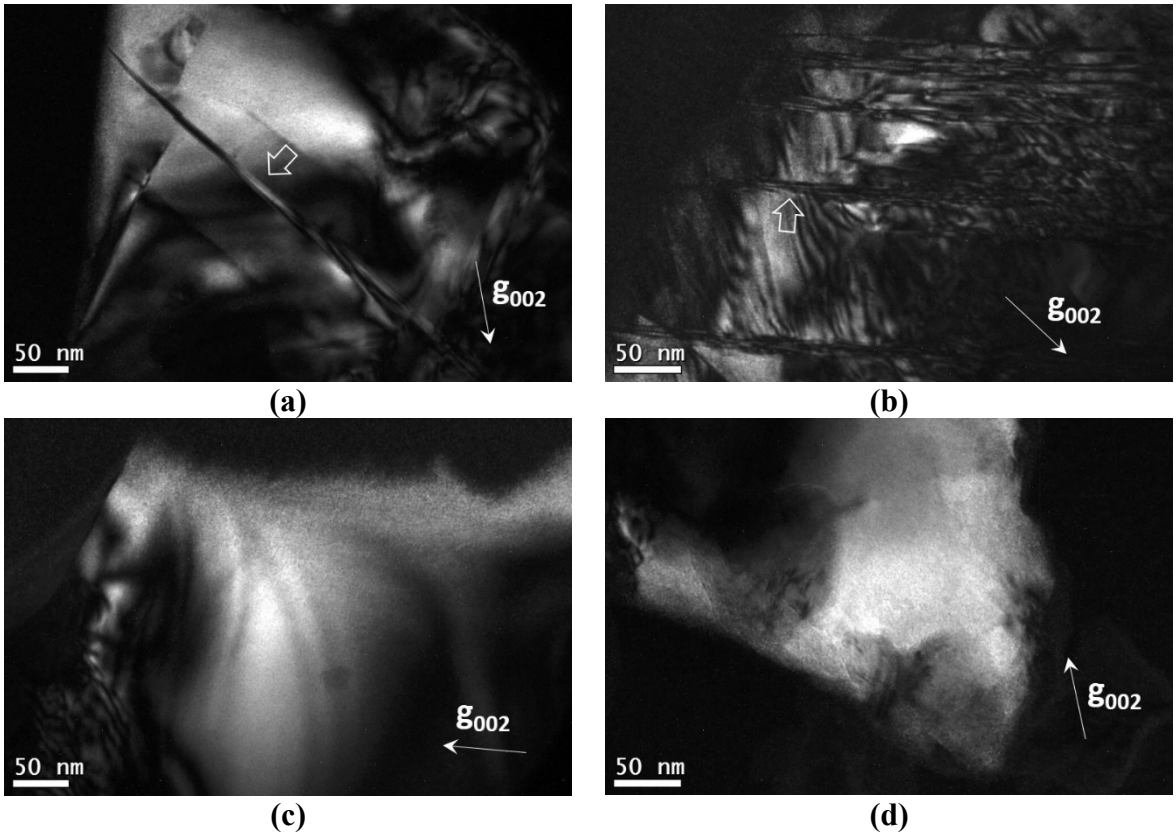

Figure 5: (a) and (b) are **g** = 002 dark field images of the $Cu_2ZnSnSe_4$ powder sample annealed at 250°C, while (c) and (d) are the corresponding images for the 100°C annealed sample. The arrows in (a) and (b) mark the location of exemplar ¼[201] (101) anti-site boundaries.

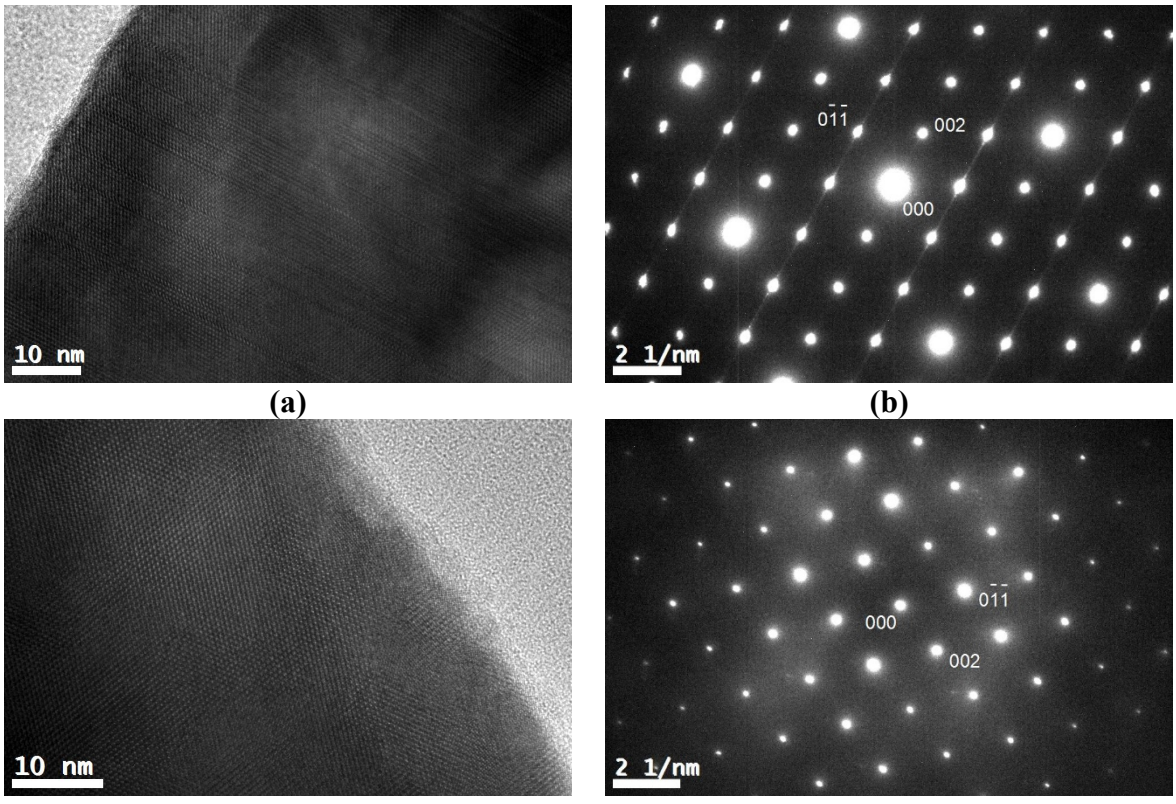

(c) **(d)**

Figure 6: (a) [010] HREM image of the 250°C annealed $Cu_2ZnSnSe_4$ sample and (b) the corresponding selected area electron diffraction pattern. ½[110] (001) anti-site boundaries are visible end-on in (a) and give rise to the streaking along the 002 reciprocal vector direction in (b). The [010] HREM image and selected area electron diffraction pattern for the 100°C annealed $Cu_2ZnSnSe_4$ sample are shown in (c) and (d) respectively. No defects are observed for this sample. The grey scale in (b) and (d) has been adjusted to reveal the presence (or absence) of any streaking.

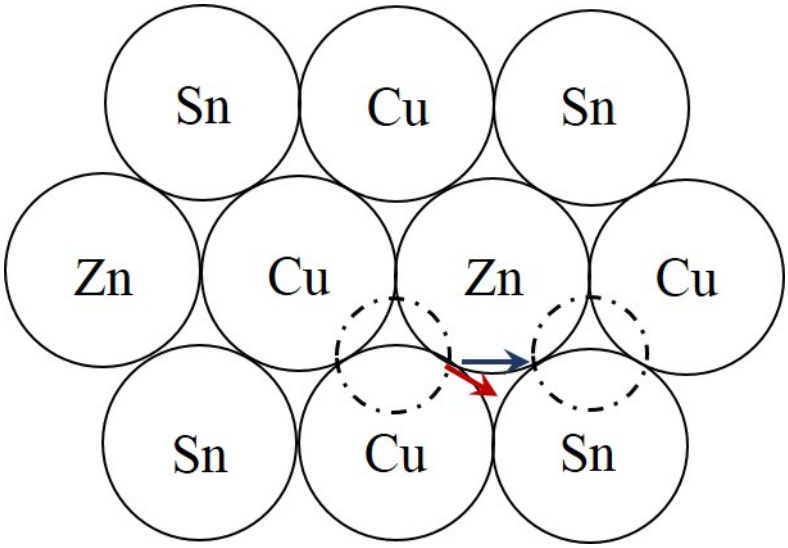

Figure 7: Schematic structure of the {112} close packed cation plane in kesterite. The top and bottom rows consist of 2a (Cu) and 2b (Sn) sites, while the middle row contains the 2c (Cu) and 2d (Zn) sites. The dashed circle represents a cation on the upper close packed plane which is displaced by ½[110] along the blue arrow to its new position on the right. The nearest neighbour cations are altered as a result of the displacement. The red arrow represents an alternative 1/12[241] shear.

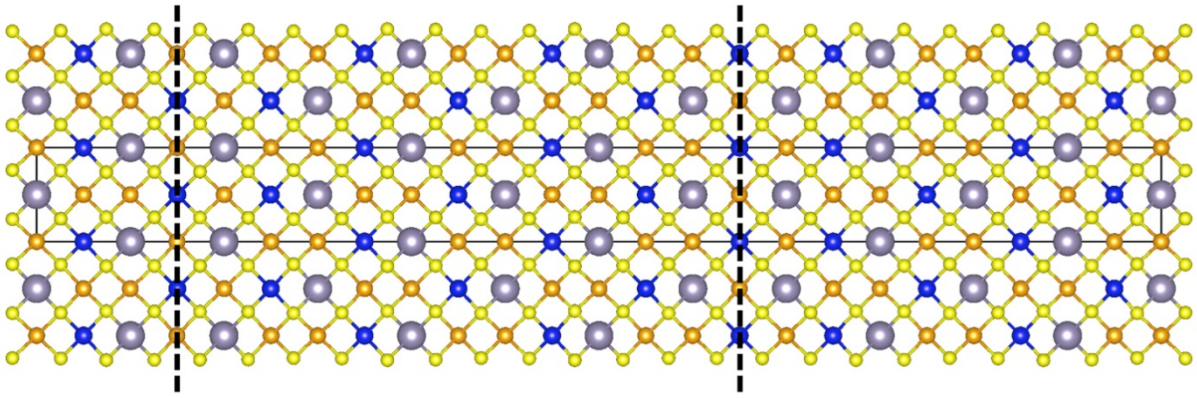

Figure 8: Optimised structure of the ½[110] (001) ASB in $Cu_2ZnSnSe_4$. The dashed lines highlight the periodically repeated ASBs. Orange, blue, silver and yellow spheres represent Cu, Zn, Sn and Se atoms respectively.

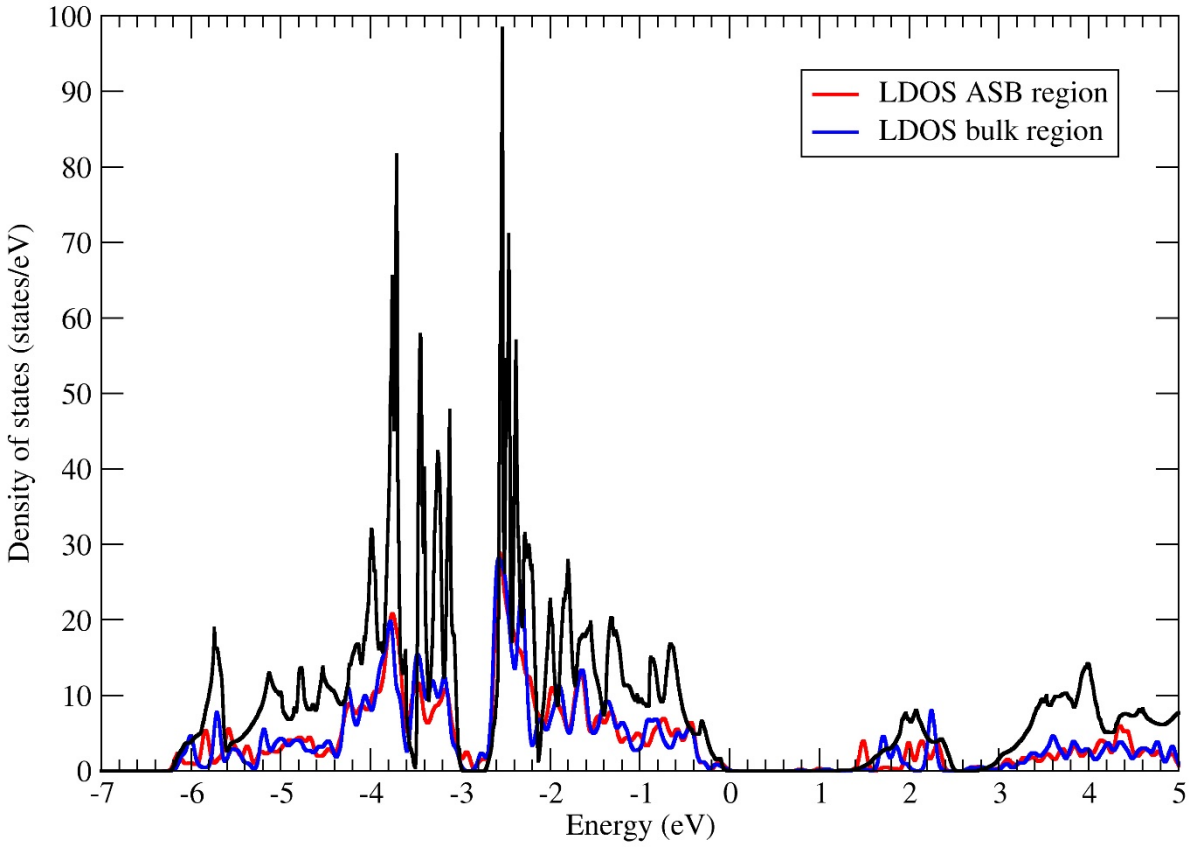
LDOS ASB region
LDOS bulk region
Density of states (states/eV)
Energy (eV)
100
90
80
70
60
50
40
30
20
10
0
-7
-6
-5
-4
-3
-2
-1
0
1
2
3
4
5

(a)

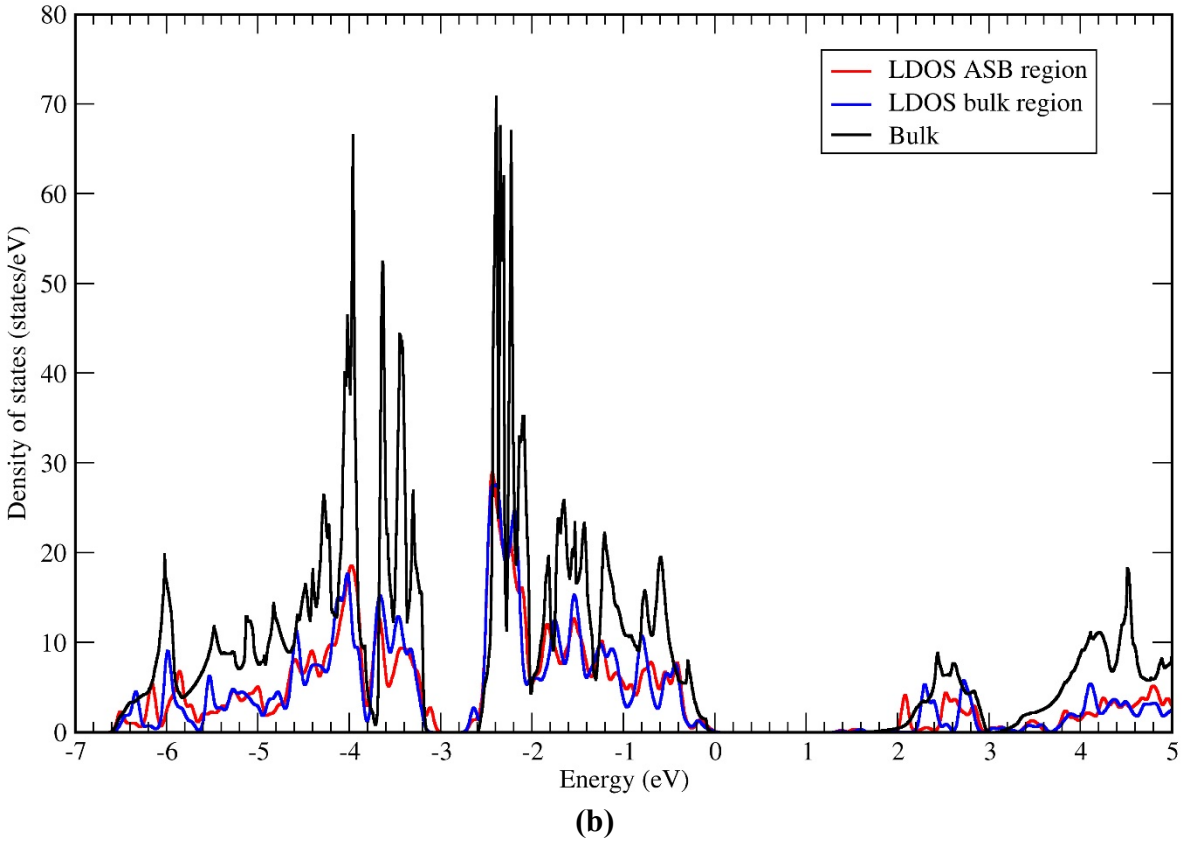
LDOS ASB region
LDOS bulk region
Bulk
Density of states (states/eV)
Energy (eV)
80
70
60
50
40
30
20
10
0
-7
-6
-5
-4
-3
-2
-1
0
1
2
3
4
5

(b)

Figure 9: Density of states of the ½[110] (001) ASB in (a) $Cu_2ZnSnSe_4$ and (b) Cu_2ZnSnS_4. The red and blue lines show the local density of states (LDOS) for the ASB and bulk regions respectively. The black line shows the total density of states for the perfect bulk crystal. Note that the bulk density of states curve resolves much finer details as the smaller cell size (16 atoms) permits a finer Monkhorst-Pack grid to be used together with the tetrahedron method for Brillouin zone integration.